Validation of a closure model framework for turbulent bubbly two-phase flow in different flow situations

Krepper, E.; Rzehak, R.; Lucas, D.;

Originally published:

October 2018

Nuclear Engineering and Design 340(2018), 388-404

DOI: https://doi.org/10.1016/j.nucengdes.2018.09.042

Perma-Link to Publication Repository of HZDR:

https://www.hzdr.de/publications/Publ-27691

VALIDATION OF A CLOSURE MODEL FRAMEWORK FOR TURBULENT BUBBLY TWO-PHASE FLOW IN DIFFERENT FLOW SITUATIONS

Eckhard Krepper, Roland Rzehak, Dirk Lucas
Helmholtz-Zentrum Dresden-Rossendorf e. V.
Institute of Fluid Dynamics, 01314 Dresden, Germany, www.hzdr.de
E.Krepper@hzdr.de

Keywords: CFD, two phase flow, Euler-Euler, closure model, validation

ABSTRACT

In the present paper a set of closure relations for interphase momentum exchange and for bubble-induced turbulence within the Euler-Euler framework is presented and validated against a set of tests performed at the HZDR-facility MT-Loop. The facility was equipped with wire-mesh sensors that allow cross sectional distributions of gas fraction, gas velocity, and bubble sizes to be measured at different distances from the gas injection.

The radial gas fraction profile of fully developed turbulent vertical upward bubbly flow in a pipe is the result of the ratio of the radial force components of the so-called non-drag forces and can be used for model validation. However, only the ratio, not the absolute value of the bubble forces can be tested in this way. In the present paper more detailed information from the experiment is exploited by consideration of the evolution of gas fraction distribution particularly after the gas injection region. The change of cross sectional gas volume fraction distribution is the result of the action of non-drag forces.

In addition to vertical pipe flow tests further insight is obtained from the investigation of the effect of a slight tube inclination which shifts the gas distribution. Here the disturbance of the cylindrical symmetry of a vertical pipe gives hints on the absolute value of the non-drag force components.

The results show that the presented model framework at least is able to describe the phenomena qualitatively. Possible reasons for quantitative deviations are discussed and require further investigations.

1. INTRODUCTION

Multiphase flows occur in a great variety of natural phenomena and technical processes. Gaining an understanding of such flows is challenging due to the complex physics involved and due to the broad range of relevant length scales. In this situation computational fluid dynamics (CFD) simulation is an important tool for both analysis and prediction. The development of suitable models for this purpose continues to be an active area of research.

A widely used approach to model two-phase bubbly flows for industrial applications is the Eulerian two-fluid framework of interpenetrating continua (Drew and Passmann 1998, Ishii and Hibiki, 2011, Yeoh and Tu 2010). The loss of details caused by the averaging procedure has to be compensated by consideration of additional closure relations. These concern the momentum exchange between the phases, the effect of the gaseous bubbles on liquid turbulence, and bubble breakup and coalescence. All described model aspects are coupled closely together and therefore in principle have to be considered as a whole.

In the literature a wide variety of investigations can be found where different closure models are compared to different experimental measurements but it is difficult to make a selection among them. In many cases the proposed models work well for the presented measurements but unfortunately fail for applications to other parameter regions or other flow situations.

For the development of a framework which can be applied to a large range of flow situations and conditions a set of best available sub-models was assembled as a baseline model (Lucas, 2016, Rzehak and Krepper, 2013a, 2013b, 2015, Liao et al. 2015, Rzehak et al., 2017a, 2017b). To ensure the predictive capabilities of the framework any case by case tuning has to be avoided. Instead it has to be shown that this model framework is able to describe different flow situations without any adaption of model details (Rzehak et al. 2017a, Ziegenhein et al., 2017). In this way, a solid foundation for the inclusion of more complex physics such as heat transfer, phase change and boiling (Krepper et al, 2011, 2013) as well as mass transfer and chemical reaction (Rzehak and Krepper, 2016, Krauß and Rzehak, 2018) is obtained.

Concerning adiabatic turbulent bubbly flow a lot of work was directed towards the investigation of vertical upward flow in a pipe. Here the boundary conditions are well defined and the experiments are very well suited to validate the closures for momentum exchange between the phases. Besides the drag forces the non-drag forces have a sensitive influence on the radial gas fraction distribution. The non-drag forces commonly comprise shear lift, wall-lift, turbulent dispersion and virtual mass forces. Comparing measured and calculated gas fraction profiles for a developed two-phase flow the ratio of the radial components of non-drag forces perpendicular to the flow direction can be validated. In the literature many experimental investigations and validation studies of this kind can be found. Representative of this type of investigation, here the experiments at MT-Loop, operated at HZDR are presented and compared to calculations (see section 5).

In the present paper these investigations of vertical upward two-phase flow are extended to get information also about the absolute value of the non-drag forces. At the MT-Loop facility the gas was injected by nozzles. In the measurements shortly behind the injection the signature of the single nozzles can be observed in the wire-mesh signals. With increasing distance from the gas injection this signature is smeared out. This smearing out effect is used to validate the model framework (see section 6).

Further investigations are performed with slightly inclined pipes, were the cylindrical symmetry is broken (see section 7). The inclination angle was set very small and only tests with limited gas

fractions were considered to ensure that the flow even at the end of the pipe is still bubbly and no larger gas fractions occur.

To facilitate a detailed analysis of the forces acting on the bubbles, it is advantageous to consider only tests with limited gas fraction so that in a preliminary first step bubble coalescence and breakup can be neglected. Only one gas phase represented by one averaged bubble size is considered. To consider hydrostatic effects the bubble size is modelled dependent on the pressure.

2. THE MODELS

A large part of work on adiabatic bubbly flow has been concerned with the forces acting on the bubbles which need to be expressed in terms of the average flow parameters by means of analytical or empirical correlations to achieve closure (e.g. Lucas et al. 2007, Rzehak et al. 2012). More recent work was focussed on bubble-induced turbulence, the effects of which are included by means of source terms in the equations for k and ε/ω of the respective turbulence models (e.g. Rzehak and Krepper 2013b, 2013c, Ma et al. 2017).

Of course, closure for bubble forces, bubble-induced turbulence and bubble coalescence and breakup cannot be considered independently in general. This is an unfortunate situation for model validations since any inaccuracy in one of the sub-models will impede qualification of all other sub-models. Therefore it is highly advantageous if some decoupling of the different phenomena can be achieved. This is possible by resorting to a monodisperse approximation for the bubble size distribution which eliminates the need to consider bubble coalescence and breakup processes.

2.1. Bubble forces

2.1.1. Drag

The drag force reflects the resistance opposing bubble motion relative to the surrounding liquid. The corresponding gas-phase momentum source is given by

$$\mathbf{F}_{DRAG} = -\frac{3}{4d_B} C_D \rho_L \alpha_G \left|\mathbf{u}_G - \mathbf{u}_L\right| \left(\mathbf{u}_G - \mathbf{u}_L\right) \tag{1}$$

The drag coefficient C_D depends strongly on the Reynolds number Re and for deformable bubbles also on the Eötvös number Eo but turns out to be independent of Morton number Mo. A correlation distinguishing different shape regimes has been suggested by Ishii and Zuber (1979), namely

$$C_D = \max\left(C_{D,sphere}, \min\left(C_{D,ellipse}, C_{D,cap}\right)\right) \tag{2}$$

where

$$\begin{aligned} C_{D,sphere} &= \frac{24}{\mathrm{Re}}\left(1 + 0.1\ \mathrm{Re}^{0.75}\right) \\ C_{D,ellipse} &= \frac{2}{3}\sqrt{\mathrm{Eo}} \\ C_{D,cap} &= \frac{8}{3} \end{aligned} \tag{3}$$

This correlation was compared with an extensive data set on the terminal velocity of bubbles rising in quiescent liquids covering several orders of magnitude for each of *Re, Eo* and *Mo* in (Tomiyama et al. 1998) with good agreement except at high values of *Eo*.

2.1.2. Lift

A bubble moving in an unbounded shear flow experiences a force perpendicular to the direction of its motion. The momentum source corresponding to this shear lift force, often simply referred to as lift force, can be calculated as (Zun 1980):

$$\mathbf{F}_{LIFT} = -C_L \rho_L \alpha_G \left(\mathbf{u}_G - \mathbf{u}_L\right) \times rot(\mathbf{u}_L) \tag{4}$$

For a spherical bubble the shear lift coefficient C_L is positive so that the lift force acts in the direction of decreasing liquid velocity, i.e. in case of co-current pipe flow in the direction towards the pipe wall. Experimental and numerical investigations showed that the direction of the lift force changes its sign if a substantial deformation of the bubble occurs. From the observation of the trajectories of single air bubbles rising in simple shear flow of a glycerol water solution the following correlation for the lift coefficient was derived (Tomiyama et al. 2002):

$$C_L = \begin{cases} \min[0.288\tanh(0.121\mathrm{Re}),\ f(Eo_\perp)] & Eo_\perp < 4 \\ f(Eo_\perp) & \text{for} \quad 4 < Eo_\perp < 10 \\ -0.27 & 10 < Eo_\perp \end{cases} \qquad (5)$$

$$\text{with} \quad f(Eo_\perp) = 0.00105Eo_\perp^3 - 0.0159Eo_\perp^2 - 0.0204Eo_\perp + 0.474$$

This coefficient depends on the modified Eötvös number given by

$$Eo_\perp = \frac{g(\rho_L - \rho_G)d_\perp^2}{\sigma} \qquad (6)$$

where $d_\perp$ is the maximum horizontal dimension of the bubble. It is usually calculated using an empirical correlation for the aspect ratio by Wellek et al. (1966) with the following equation:

$$d_\perp = d_B \sqrt[3]{1 + 0.163 \cdot Eo^{0.757}} \qquad (7)$$

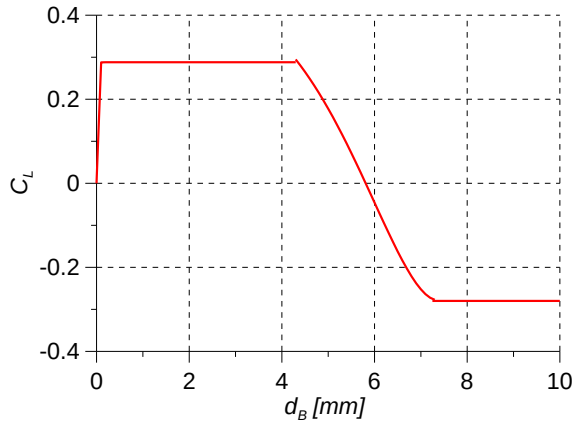

Figure 1: Lift coefficient C_L dependent on bubble size d_B for air/water bubbly flow (Eq. 5)

For air/water bubbly flow at normal conditions the sign change of the lift coefficient occurs at a bubble size of about $d_B \approx 6$ mm (see Figure 1). For steam-water flow at higher pressure the correlations Eq. (5) to (7) yield smaller critical bubble sizes which could be confirmed by investigations at the TOPFLOW facility operated at HZDR. So for a pressure of 5 MPa a critical bubble size of d_B=4 mm and for 10 MPa of d_B=3mm could be found (Lucas & Tomiyama 2011). Even for refrigerants used in subcooled boiling experiments these correlations seem to be valid. In the boiling tests at the DEBORA facility operated at CEA Dichlorodifluoromethane (R12) was used. For this fluid

the critical diameter was found for very small bubbles, e.g. at about 2.5 MPa a critical diameter of d_B=1mm was calculated and found also in the measurements (Krepper et al. 2013).

2.1.3. Wall force

A bubble translating next to a wall in an otherwise quiescent liquid also experiences a lift force. This wall lift force, often simply referred to as wall force, has the general form

$$\mathbf{F}_{WALL} = \frac{2}{d_B} C_W \rho_L \alpha_G \left|\mathbf{u}_G - \mathbf{u}_L\right|^2 \hat{\mathbf{y}} \tag{8}$$

where $\hat{y}$ is the unit normal perpendicular to the wall pointing into the fluid. The dimensionless wall force coefficient C_W depends on the distance to the wall y and is expected to be positive so the bubble is driven away from the wall.

Based on the observation of single bubble trajectories in simple shear flow of a glycerol water solution Tomiyama et al. (1995) and later Hosokawa et al. (2002) concluded a functional dependence

$$C_W(y) = f(Eo)\left(\frac{d_B}{2y}\right)^2 \tag{9}$$

In the limit of small Morton number the correlation

$$f(Eo) = 0.0217\ \ Eo \tag{10}$$

can be derived from the data of Hosokawa et al. (2002). The experimental conditions on which Eq. (10) is based are 2.2 ≤ Eo ≤ 22 and log10 Mo = -2.5 … -6.0 which is still different from the water-air system with Mo = 2.63e-11 but a recent investigation (Rzehak et al. 2012) has nonetheless shown that good predictions are obtained also for air bubbles in water.

2.1.4. Turbulent dispersion force

The turbulent dispersion force describes the effect of the turbulent fluctuations of liquid velocity on the bubbles. Burns et al. (2004) derived an explicit expression by Favre averaging the drag force as:

$$\mathbf{F}_{DISP} = -\frac{3}{4} C_D \frac{\alpha_G}{d_B} \left|\mathbf{u}_G - \mathbf{u}_L\right| \frac{\mu_L^{turb}}{\sigma_{TD}} \left(\frac{1}{\alpha_L} + \frac{1}{\alpha_G}\right) \mathrm{grad}\, \alpha_G \tag{11}$$

In the same work the expression for the so-called Favre averaged drag (FAD) model has also been compared with other suggestions which all agree at least in the limit of low gas fraction.

In analogy to molecular diffusion, σ_{TD} is referred to as a Schmidt number. In principle it should be possible to obtain its value from single bubble experiments also for this force by evaluating the statistics of bubble trajectories in well characterized turbulent flows but to our knowledge this has not been done yet. A value of σ_{TD} = 0.9 is typically used.

It should be mentioned here that the turbulent dispersion force $\mathbf{F}_{DISP}$ represents a sensitive influence of the turbulence of the continuous liquid phase on the distribution of the dispersed gas fraction. The

turbulent viscosity μ_L^{turb} in Eq. (11) is influenced by the approach for bubble-induced turbulence described in section 2.2.

2.1.5. Virtual mass

When a bubble is accelerated, a certain amount of liquid has to be set into motion as well. This may be expressed as a force acting on the bubble as

$$\mathbf{F}_{VIRM} = -C_{VM}\rho_L\alpha_G\left(\frac{D_G\mathbf{u}_G}{Dt} - \frac{D_L\mathbf{u}_L}{Dt}\right) \tag{12}$$

where D_G / Dt and D_L / Dt denote material derivatives with respect to the velocity of the indicated phase. For the virtual mass coefficient C_{VM} a value of 0.5 has been derived for isolated spherical bubbles in inviscid and creeping flows by Auton et al. (1988) and Maxey and Riley (1983), respectively. Results of direct simulations of a single bubble by Magnaudet et al. (1995) suggest that this value also holds for intermediate values of Re.

2.2. Bubble-induced turbulence

Due to the small density and small special scales of the dispersed gas it suffices to consider turbulence in the continuous liquid phase for bubbly flows. We adopt a two equation turbulence model for the liquid phase with additional source terms describing bubble-induced turbulence. The formulation given is equally applicable to either k-ε, k-ω or SST model, but the latter SST-model (Menter 1994, 2009) will be used presently.

Concerning the source term describing bubble effects in the k-equation there is large agreement in the literature. A plausible approximation is provided by the assumption that a large part of the energy lost by the bubble due to drag is converted to turbulent kinetic energy in the wake of the bubble. Hence, the k-source becomes

$$S_L^k = C_{kB}\mathbf{F}_L^{drag}\cdot\left(\mathbf{u}_G - \mathbf{u}_L\right) \tag{13}$$

For the ε-source a similar heuristic is used as for the single phase model, namely the k-source is divided by some time scale τ so that

$$S_L^\varepsilon = C_{\varepsilon B}\frac{S_L^k}{\tau} \tag{14}$$

Further modeling then focuses on the time scale τ proceeding largely based on dimensional analysis. This follows the same line as the standard modeling of shear-induced turbulence in single phase flows (Wilcox 1998), where production terms in the ε-equation are obtained by multiplying corresponding terms in the k-equation by an appropriate time scale which represents the life-time of a turbulent eddy before it breaks up into smaller structures. In single phase turbulence the relevant variables are obviously k and ε from which only a single time scale $\tau = k_L/\varepsilon_L$ can be formed. Rzehak and Krepper (2013c) have extended these considerations for the more complex situations of bubble-induced turbulence in two-phase flows. Obviously there are two length (d_B and $k_L^{3/2}/\varepsilon_L$) and two velocity scales ($\left|U_G - U_L\right|$ and $\sqrt{k_L}$) in the problem, where one of each is related to the bubble and the other to the turbulent eddies. In principle a total of four different time scales relating a length

scale to a velocity scale can be formed. Different possibilities were investigated yielding different agreement to measurements and different numerical stability.

A more recent investigation (Ma et al. 2017) used direct numerical simulations to derive closures for the bubble-induced turbulence. There for the relaxation time

$$\tau = \frac{d_B}{\left|\mathbf{u}_G - \mathbf{u}_L\right|} \tag{15}$$

was applied. The comparison to the direct numerical simulations yielded for the coefficients C_{kB} and $C_{\varepsilon B}$ in Eq. (13) and (14):

$$C_{kB} = \min\left(0.18\,\mathrm{Re}^{0.23}, 1\right) \tag{16}$$

and

$$C_{\varepsilon B} = 0.3 C_D \tag{17}$$

For use with the SST model, the ε-source is transformed to an equivalent ω-source which gives

$$S_L^{\omega} = \frac{1}{C_{\mu} k_L} S_L^{\varepsilon} - \frac{\omega_L}{k_L} S_L^{k} \tag{18}$$

This ω-source is used independently of the blending function in the SST model since it should be effective throughout the fluid domain.

Since bubble-induced effects are included in k and ε / ω due to the respective source terms, the turbulent viscosity is evaluated from the standard formula

$$\mu_L^{\,turb} = C_{\mu} \rho_L \frac{{k_L}^2}{\varepsilon_L} \tag{19}$$

The effective viscosity is simply $\mu_L^{eff} = \mu_L^{mol} + \mu_L^{turb}$

Boundary conditions on k and ε / ω are taken the same as for single phase flows, which is consistent with the view that the full wall shear stress is exerted by the liquid phase which contacts the full wall area. A single phase wall function is employed to avoid the need to resolve the viscous sublayer. All turbulence model parameters take their usual single phase values for the presently investigated tests.

3. THE EXPERIMENTS AT THE MT-LOOP TEST FACILITY

At the MT-Loop experiments air bubbles were injected in an upward vertical water flow in a round pipe. The pipe had an inner diameter of 51.2 mm and a length of more than 3 m. The general arrangement is shown in Figure 2. Wire-mesh sensor measurements were performed by two subsequent sensors at 36 mm distance. By the sensors the cross sectional distribution of gas fraction and the bubble size distribution was measured. Correlating the signals of lower and upper sensor the cross sectional distribution of the gas velocity was determined. In addition pressure measurements were taken at the position of the wire-mesh sensor. Air at normal temperature was injected by nozzles having a diameter of 1 mm distributed over the cross section of the pipe (see Figure 3). Depending on the gas flow rate a different number of nozzles were activated. Different tests with the same flow boundary conditions but different distances from the gas injection to the wire-mesh sensors were performed. Table 1 shows the investigated distances from gas injection to measurement plane. Assuming the same boundary conditions during all tests of a series, the flow development can be observed (see Lucas et al. 2005).

Tests were conducted for different values of gas and liquid flow rates as listed in Table 2 for normal conditions of pressure and temperature. Parameters to be imposed at the inlet are also shown. Their determination form the measurements will be discussed in the next section.

In addition to tests where the pipe was oriented vertically, also tests with a small inclination angle were performed. Different values of the inclination were considered, i.e. 0, 6.4, 12.8 and 25.6 mm/m. In all of these cases the flow still remained in the bubbly regime up to the end of the test section.

Table 1: Investigated distances x from gas injection to measurement plane [m]

A	B	C	D	E	F	H	I	K	L
0.03	0.08	0.13	0.23	0.43	0.83	1.53	2.03	2.53	3.03

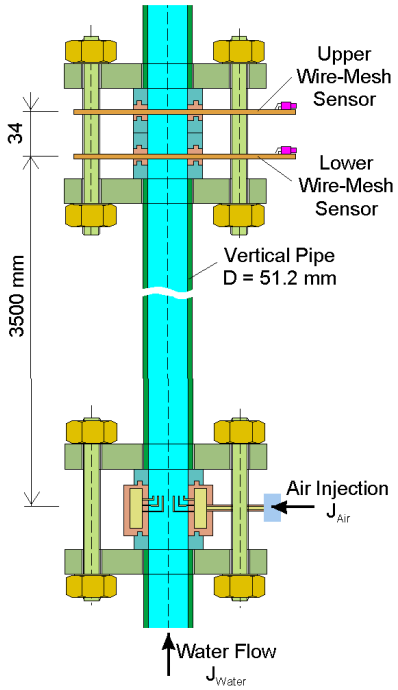

Figure 2: Arrangement of air injection and wire-mesh sensor during the MT-Loop tests

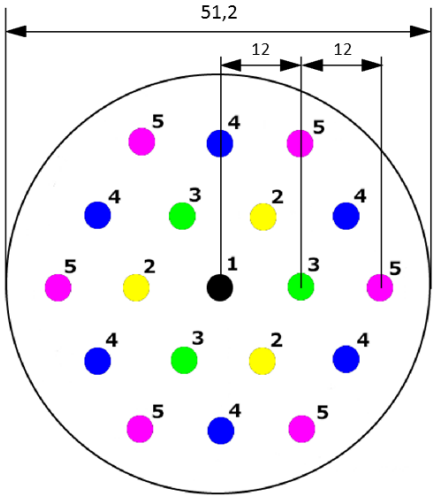

Figure 3: Distribution of the 19 nozzles over the cross section (compare Figure 2 air injection)

4. CFD-SETUP AND DEFINITION OF BOUNDARY CONDITIONS

In all of the present simulations the full 3D geometry is modelled. Figure 4 shows the schema of the numerical setup. The x-axis is taken along the direction of the vertical flow. The pipe length is set from x=-1 m until x=3.3 m. The reference grid GRDRef consists of ca. 470000 elements. A grid resolution study is presented in section 6.3. The specified fluids are water for the liquid phase and compressible air ideal gas for the gaseous phase. Figure 4 presents the gas fraction at a central xz-plane for the test MT-050. The liquid enters by an inlet from below assuming a turbulent flow profile for the velocity

$$U_L = U_{AV}\left(1-\frac{r}{R}\right)^{1/6} \tag{20}$$

and a developed flow profile for liquid turbulent kinetic energy and liquid eddy dissipation gained from a previous single phase calculation. The gas injection is modelled by point sources at x=0 m (see Figure 4). Positions of the point sources in the yz-plane correspond to the locations of the inlet nozzles in the experiment (see Figure 3). At the top a pressure boundary is set. Wall functions like for single phase liquid flow are used.

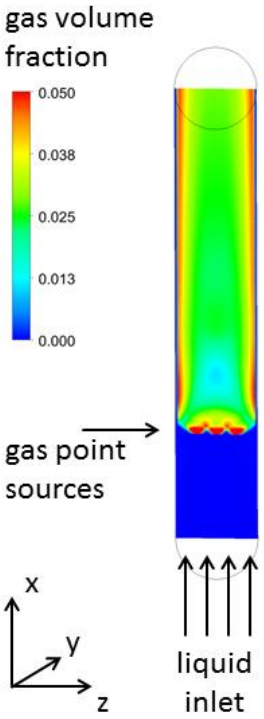

Figure 4: Calculated gas fraction in the xz-plane for test MT-050

In the MT-Loop tests pressures of about 0.11 MPa and 0.14 MPa were measured at the outlet and inlet positions, respectively. As a consequence of the decrease in hydrostatic pressure between inlet and outlet, the gas density and bubble size change along the vertical direction according to

$$\rho_G(P) = \rho_{G,REF}\,\frac{P}{P_{REF}} \qquad d_B(P) = d_{B,REF}\sqrt[3]{\frac{P_{REF}}{P}} \tag{21}$$

In the calculations this effect is included by varying both quantities accordingly.

Table 2: Parameters of the investigated tests									
	028	**039**	**041**	**050**	**052**	**061**	**063**	**083**	**085**
Nozzle groups	2	2+3	2+3	1+2+3	1+2+3	all	all	all	all
j_L [m/s]	0.405	0.405	1.017	0.405	1.017	0.405	1.017	0.405	1.017
j_G [m/s]	0.0062	0.0096	0.0096	0.0151	0.0151	0.0235	0.0235	0.0574	0.0574
$j_{G,IN}$ [m/s]	0.0058	0.0092	0.0101	0.0169	0.0165	0.0259	0.0257	0.0694	0.0691
$d_{B,IN}$ [mm]	4.054	3.861	3.450	4.208	3.743	3.945	3.945	5.135	4.572

Table 2 presents the parameters of the investigated tests. For the location of the activated nozzle groups compare Figure 3. Superficial velocities of the considered tests are given. Here j_L and j_G describe the specified values of the test matrix for normal conditions of pressure and temperature. For the actual simulations the superficial velocities and the bubble size at the inlet are taken from the measurements in the following way. Cross sectionally averaged gas fractions and gas velocities and resulting superficial gas velocities are determined from the measurements for the different height levels. They are transformed to standard conditions for pressure and temperature by Eq. (21), averaged over all levels A to L and finally recalculated to the inlet level considering the inlet pressure. The corresponding values are given in Table 2 as $j_{G,IN}$. The same procedure is applied to the cross sectionally averaged bubble sizes. In the investigated tests the strongest changes of the bubble sizes can be observed for the levels A to D which is considered here as an inlet region (level D: x = 0.43 m). In the further course the bubble size is mainly influenced by hydrostatic effects. Deviations from it are a sign that here neglected bubble coalescence respective breakup have an influence. Here the reference bubble size is performed by fitting only for the inlet region of levels A to D and the used values for the inlet are given in Table 2 as $d_{B,IN}$.

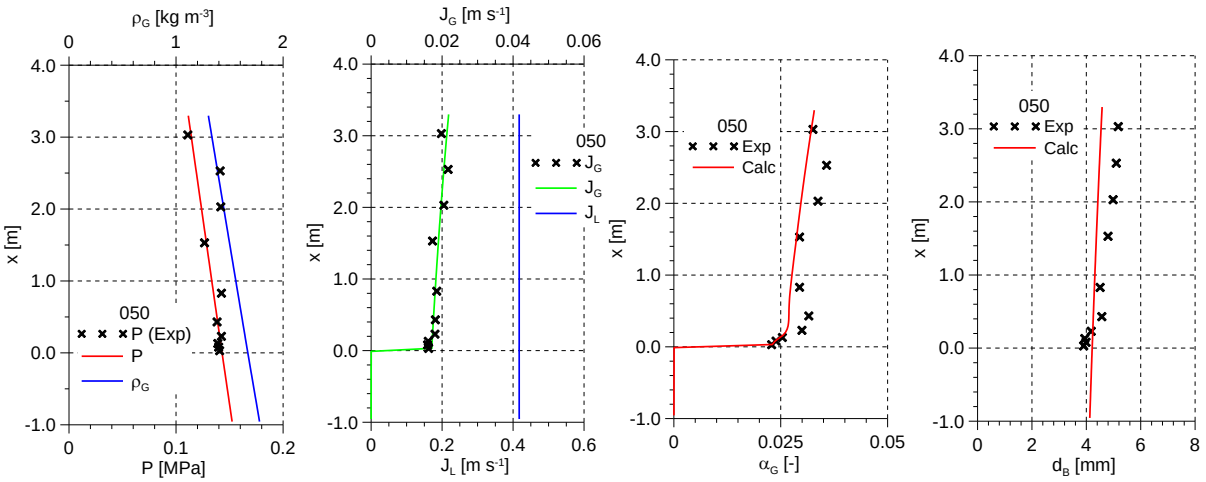

a) Pressure and gas density

b) Gas and liquid superficial velocities

c) Gas fraction

d) Bubble size

Figure 5: Vertical development of cross sectional averaged values for test MT-050

(x-axis in vertical direction)

In the pipe of a height of 3 m the hydrostatic pressure causes a bubble volume increase by 25%. For the bubble size an increase of by 8% has to be expected. Figure 5 shows this effect in both simulation and experiment by cross sectionally averaged values for the example of test MT-050. Measured bubble size deviations from this value can be explained by here neglected bubble breakup respective bubble coalescence (see Figure 5d).

In all simulations of the following sections 5, 6 and 7 the same reference mesh is applied. For all test configurations a grid resolution study was performed, which is here only presented in section 6 where the smearing of gas fraction is investigated. In this case diffusion effects caused by a too coarse grid have to be excluded and the grid independence is explicitly shown in section 6.3.

During the investigations radial calculated profiles for gas volume fraction and gas velocity at corresponding axial distances from the gas injection are compared to measurements. These calculated profiles (Figures 6, 11, 12 and 14) are determined by azimuthal averaging in the same way like in the experiments. Furthermore radial components of the non-drag forces are shown (Figures 7 and 13). These are determined along a line perpendicular to the flow direction. Considering the symmetric arrangement of the inlet nozzles for the different flow regimes (Figure 3) this probe line is directed along the z-axis.

Whereas the calculations can be performed with any CFD code, for the actual simulations ANSYS-CFX is applied.

5. TWO-PHASE DEVELOPED FLOW IN A VERTICAL PIPE

In this section, experiments with vertical upward flow of both liquid and gas are considered and the focus is on the almost fully developed flow. Figure 6 shows the gas fraction profiles at the highest level L (x=3.03 m) while in Figure 7 the corresponding radial components of the non-drag forces are presented. The virtual mass force plays no role for the developed flow conditions considered. Hence the gas fraction profiles are determined by the lift force, the wall force and the turbulent dispersion force.

The tests MT-039 MT-050 and MT-061 show a typical gas fraction profile for a vertical pipe flow consisting of small bubbles. The profile is wall peaked. Agreement between calculated and measured profiles is quite good. The radial gas distribution is determined mainly between the interplay of lift- and turbulent dispersion force against wall force (see Figure 7).

Tests MT-041, MT-052 and MT-063 also exhibit wall-peaked gas fraction profiles. However experiment and simulation agree less. In particular the calculated profiles show no gas in the pipe centre in contrast to the measured ones. From a previous investigation it is known that the consideration of fixed polydispersity is able to describe this phenomenon (Rzehak and Krepper, 2015). Here a second gaseous dispersed phase is specified representing larger bubbles. The corresponding negative lift force represents the mechanism transporting larger bubbles into the pipe centre. This mechanism is missing in the monodispersed approach in the tests listed above.

With larger gas fraction in tests MT-083 and MT-085, the turbulent dispersion force exceeds the other forces (see Figure 7), while the lift force is decreased. Here the turbulent dispersion force instead of lift force for large bubbles yields the mechanism transporting gas into the tube centre. This explains the good agreement of the volume fraction profiles for bubbly flow with higher gas fractions despite the monodisperse approximation.

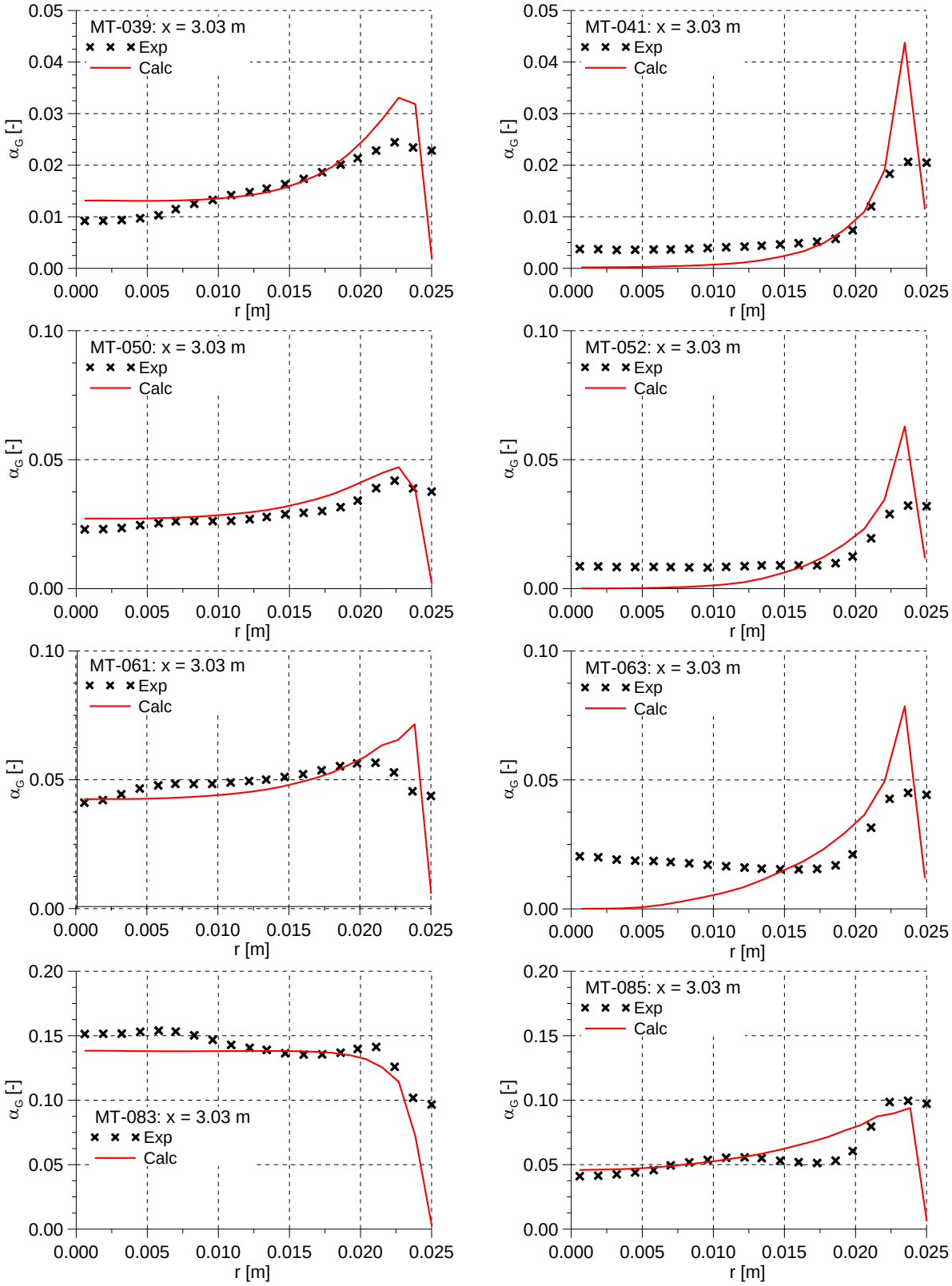

Figure 6: Comparison of radial gas fraction profiles for developed two-phase vertical upward flow (superficial velocities see Table 2)

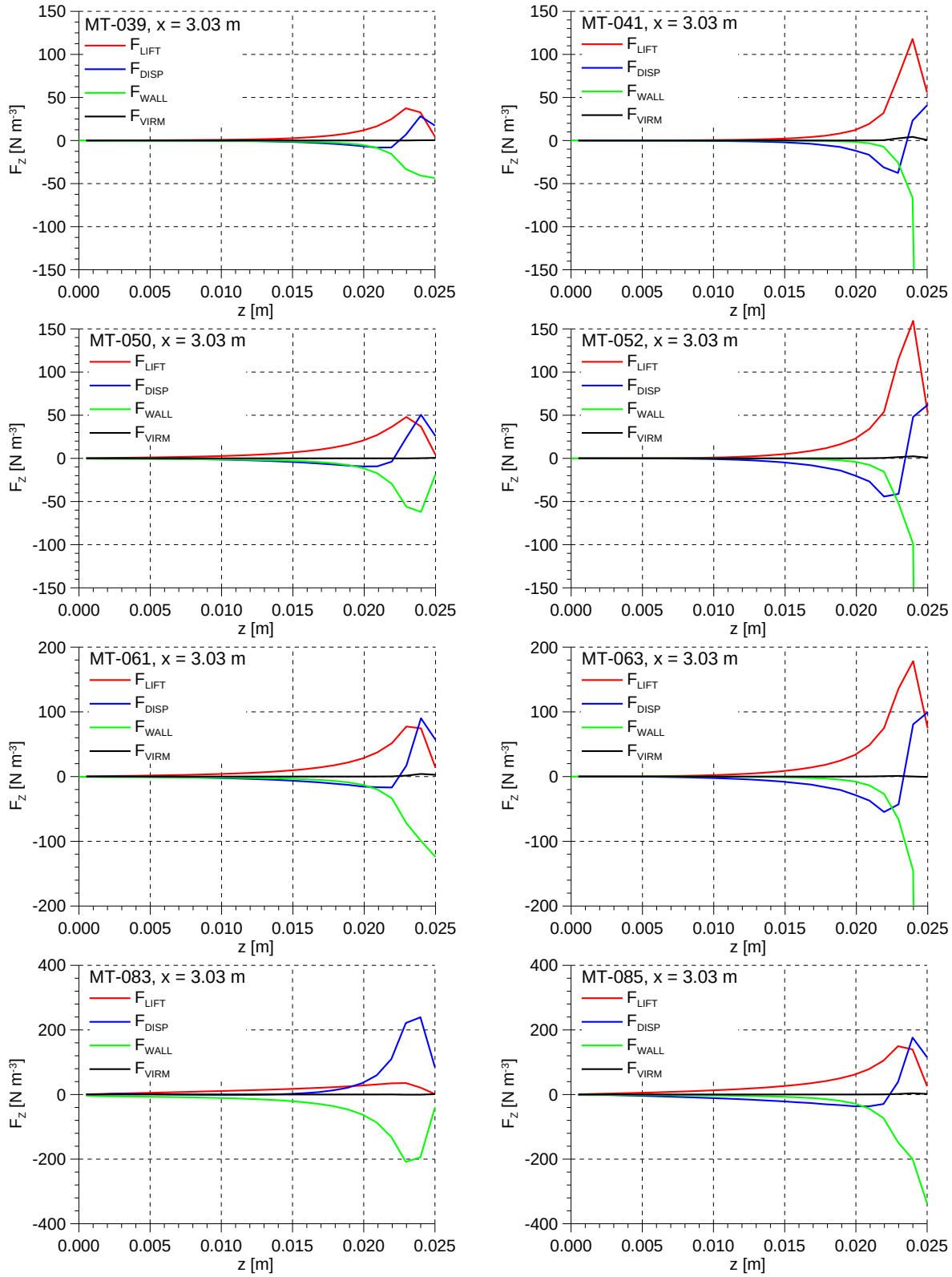

Figure 7: Radial component of the non-drag forces at level L, 3.03 m behind the gas injection

6. PHENOMENA NEAR THE GAS INJECTION

6.1. Experiments

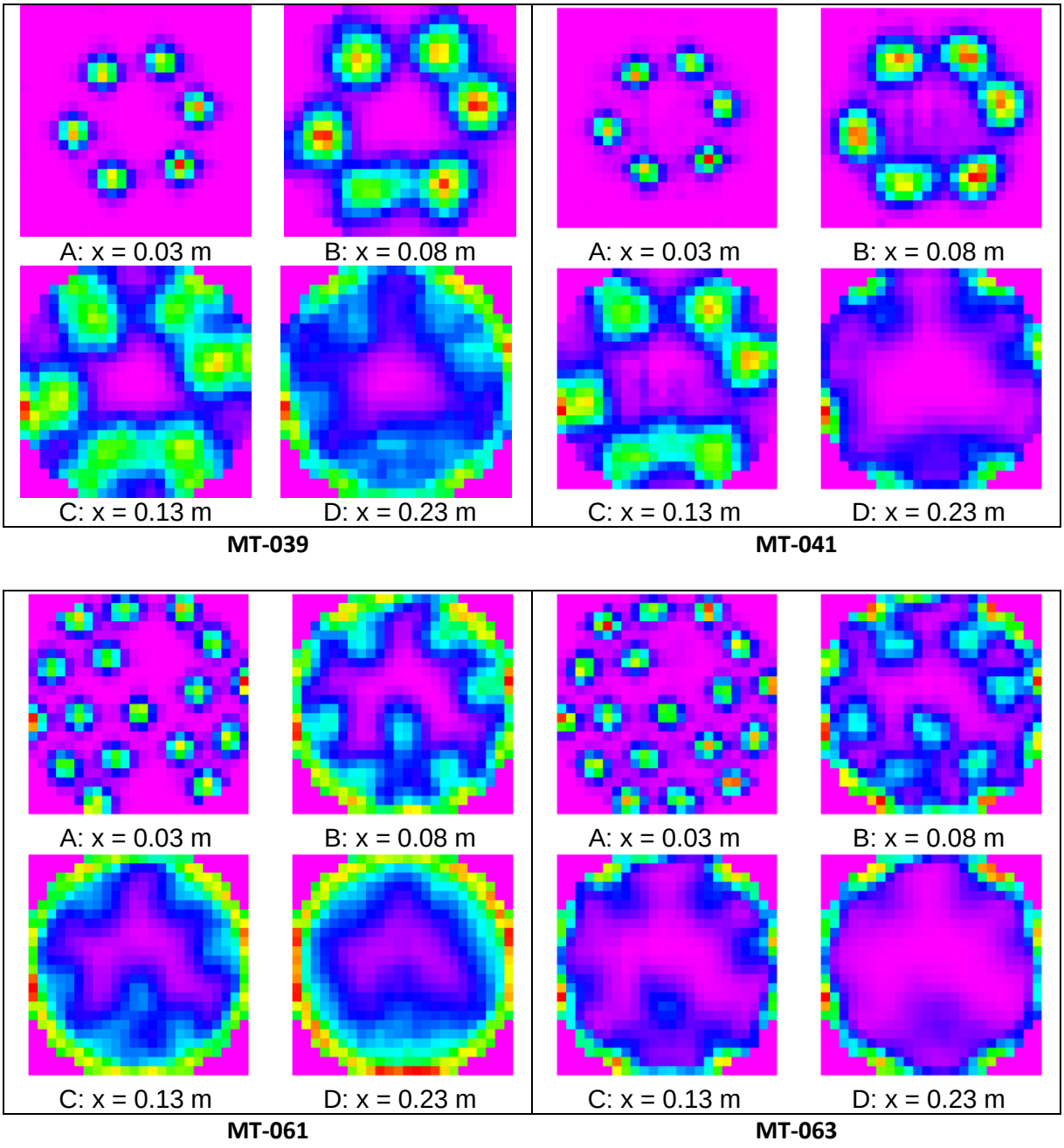

Fig 8: Measured gas gas fraction distribution at different distances x from the air injection (superficial velocities see Table 1)

The same vertical pipe experiments as in section 5 are considered but now the focus is shifted to the phenomena occurring near the gas injection. The measured cross sectional gas distributions at levels A to D are shown in Figure 8 for a selection of test conditions. Close to the injection plane (level A at x = 0.03 m) a gas fraction maximum can be found above each gas injection nozzle position. These maxima are smoothened with larger distance from the injection plane (levels B, C and D at x = 0.08,

0.13 and 0.23 m). For all tests shown, the nozzle pattern is not visible anymore at level D. Lucas et al. (2005) shows the corresponding measured gas fraction distributions for further tests and further distances from the gas injection.

6.2. Calculations and Discussion

For the simulations the same numerical setup described in section 4 is applied. To avoid the diffusive effect of a coarse grid, a quite fine resolution of the hexahedral grid particularly in the gas injection region is ensured. For the cross section here about 1000 cells in a horizontal plane are simulated. A corresponding grid resolution study is presented below in section 6.3.

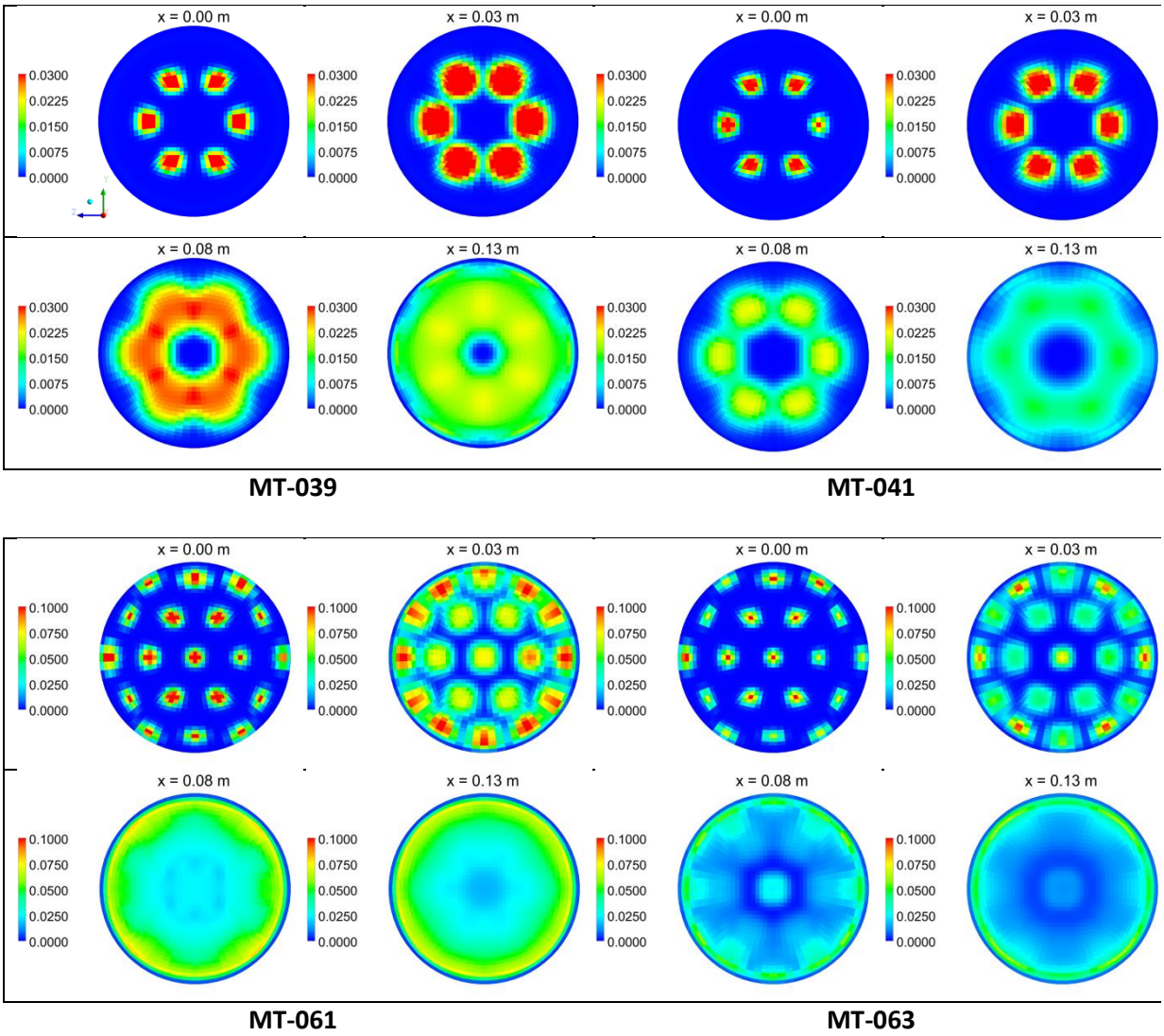

Figure 9: Calculated gas fraction distribution at different distances from the gas injection

Figure 9 shows the calculated gas fraction distribution over the pipe cross section at different distances from the injection. The disappearance of the pattern caused by the inlet nozzles with increasing distance from the inlet is in qualitative agreement with the measurement results of Figure. 8.

Radial distributions of the gas fraction are determined by azimuthal averaging corresponding to the procedure performed in the experiments. The radius R is divided into N equidistant sections. In the actual case N was selected as 32 and carefully checked to have no influence of N on the averaging result.

Comparison to the measurements is shown in Figure 10 for different distances from the inlet. For all cases although the agreement of the gas fraction profiles is quite good at x = 0.03 m, larger discrepancies can be found at x = 0.08 m and x = 0.13 m downstream of the injection. At x = 0.23 m the agreement is quite reasonable again.

The reason for this behaviour can be traced to the effect of the lift force which depends very sensitively on the liquid velocity gradients. The liquid velocity profiles shown in Figure 11 reveal an accelerating effect of the injected gas on the liquid which causes a local maximum downstream of the position of the injection nozzle. For the test MT-039, e.g., a single maximum can be found at r = 0.01m both for x = 0.03m and x = 0.08m. According to the definition of the lift force in Eq. (4) (section 2.1.2) small bubbles are directed away from the flow maximum. This explains the shifted gas fraction profiles at x = 0.08 m and x = 0.13 m. At x = 0.23 m the signature of the nozzles disappears both in measurements and calculations. For larger distances L/D these local effects are further equalized and the agreement becomes better. In other cases nozzles at different radial positions are active but show similar phenomena. The general flow characteristics, like the disappearance of the visibility of the nozzle position in the gas fraction profiles can be found in good agreement to the measurements.

Figure 12 shows the radial component of the non-drag forces at the shortest distance x = 0.03 m. Whereas the profiles for gas fraction and the velocities in Figures 10 and 11 are azimuthally averaged the profiles for the non-drag forces are determined along a line. For reasons of symmetry of the arrangement of injected nozzles this is a line parallel to the z-axis and not parallel to the y-axis (compare Figure 9). Whereas near the gas injection the main contribution of non-drag forces can be found from the lift and the virtual mass force, in the developed flow at x = 3 m (Figure 7, section 5) an equalization of lift- and wall force respective for larger gas fractions equalization of turbulent dispersion force and wall force can be found. The contribution of the virtual mass force for these developed flows could be neglected.

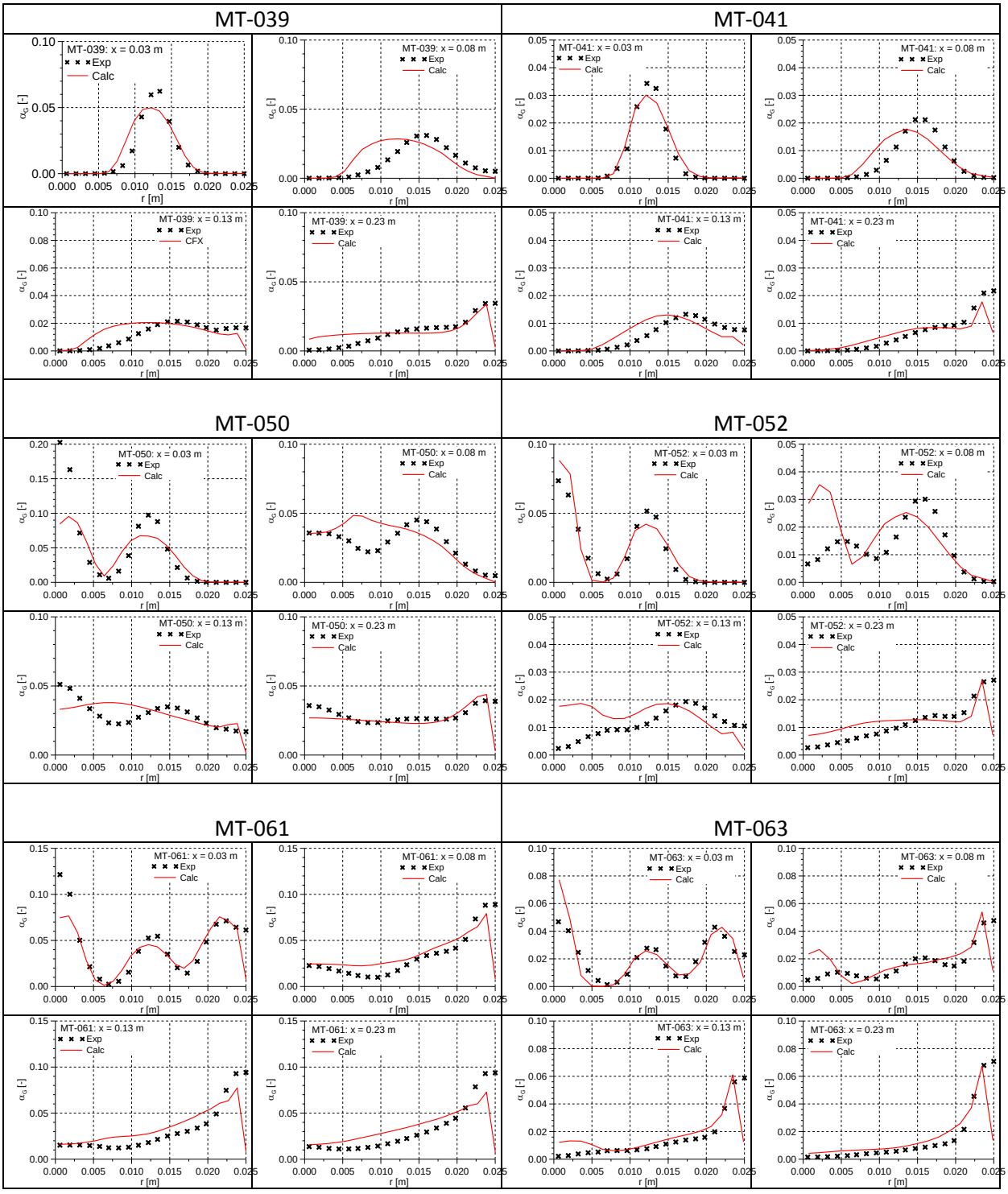

Figure 10: Measured and calculated azimuthally averaged gas fraction profiles

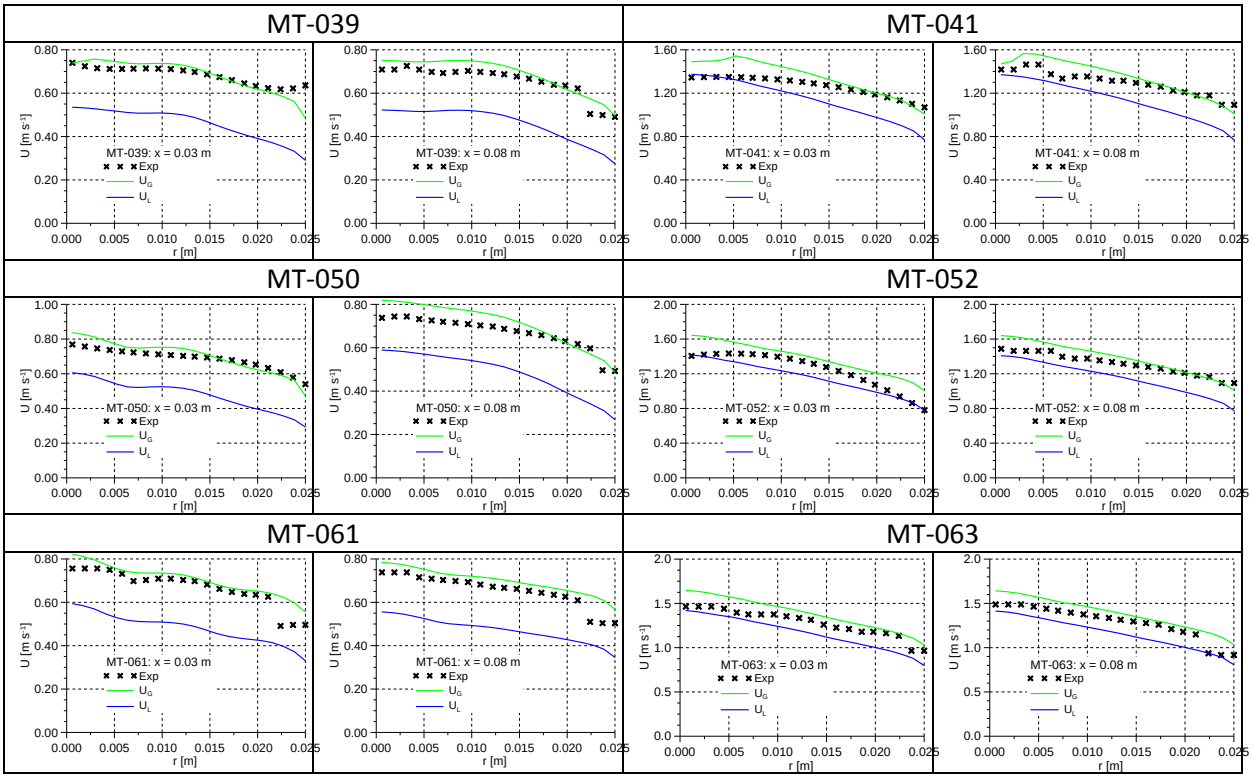

Figure 11: Measured and calculated azimuthally averaged gas and liquid velocities at 0.03 m and 0.08 m behind the gas injection

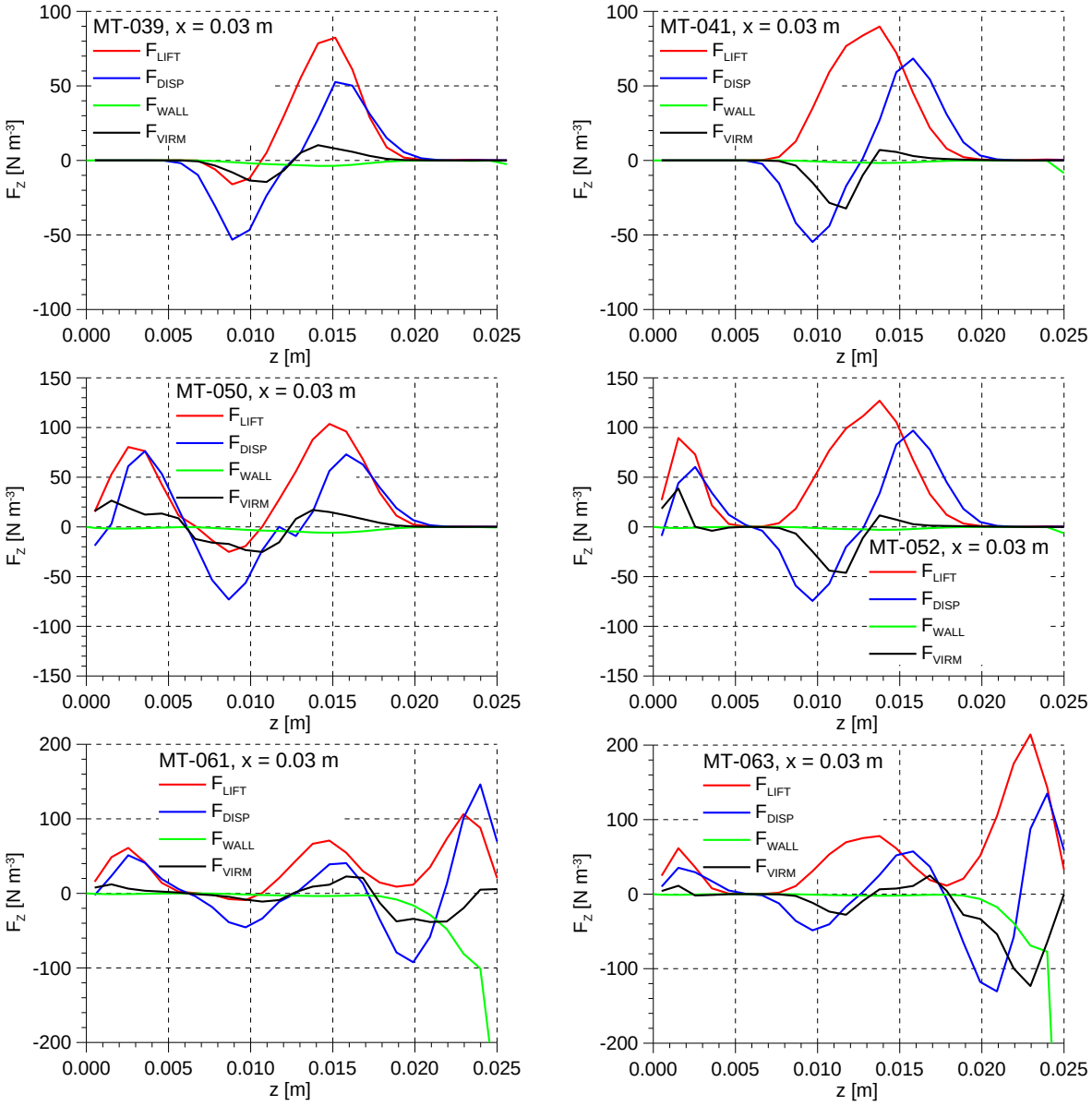

Figure 12: Radial component of non-drag forces at 0.03m behind the gas injection

6.3. Influence of the grid resolution

Grid resolution studies are performed for all cases discussed in the paper but in most cases not shown here. For the topic of section 6 grid resolution plays a special role since a possible diffusive effect of a too coarse grid has to be excluded. Therefore the grid resolution study for this chapter is explicitly presented. Whereas the reference grid GRDRef consists of ca. 470000 elements a coarser grid GRDS having ca. 75000 elements and a finer grid GRDL with ca. 2000000 elements are investigated. The gas fraction profiles shortly behind the injection and at the end of the pipe for the tests MT-039 and MT050 are shown in Figure 13. Small differences can be found in the near injection region. Never the less the main characteristics like the location of maxima are not influenced by the grid resolution.

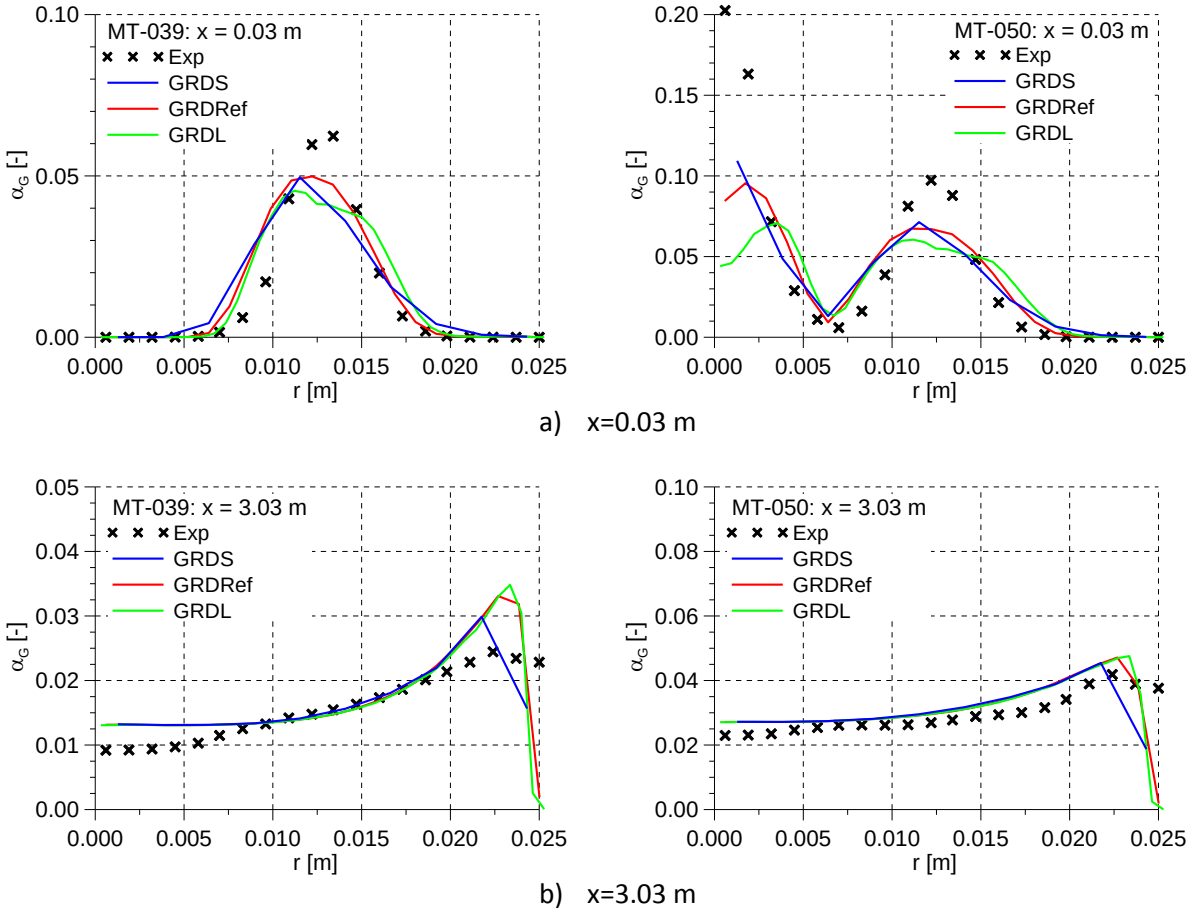

Figure 13: Radial gas fraction profiles for different grid size resolutions at two distances from the gas injection

7. SLIGHTLY INCLINED PIPE

7.1. Experiments

Here, the MT-Loop investigations with a slightly inclined pipe are considered. Figure 14 shows the measured cross sectional distribution of the gas at different inclination angles and the bubble size distribution, both 3.03 m upstream of the gas injection. The direction of pipe inclination is over the diagonal from the lower left to the upper right corner. A stronger gas accumulation in the lower left corner can be observed. This disturbance of the cylindrical symmetry can be used to validate the simulation of the non-drag forces.

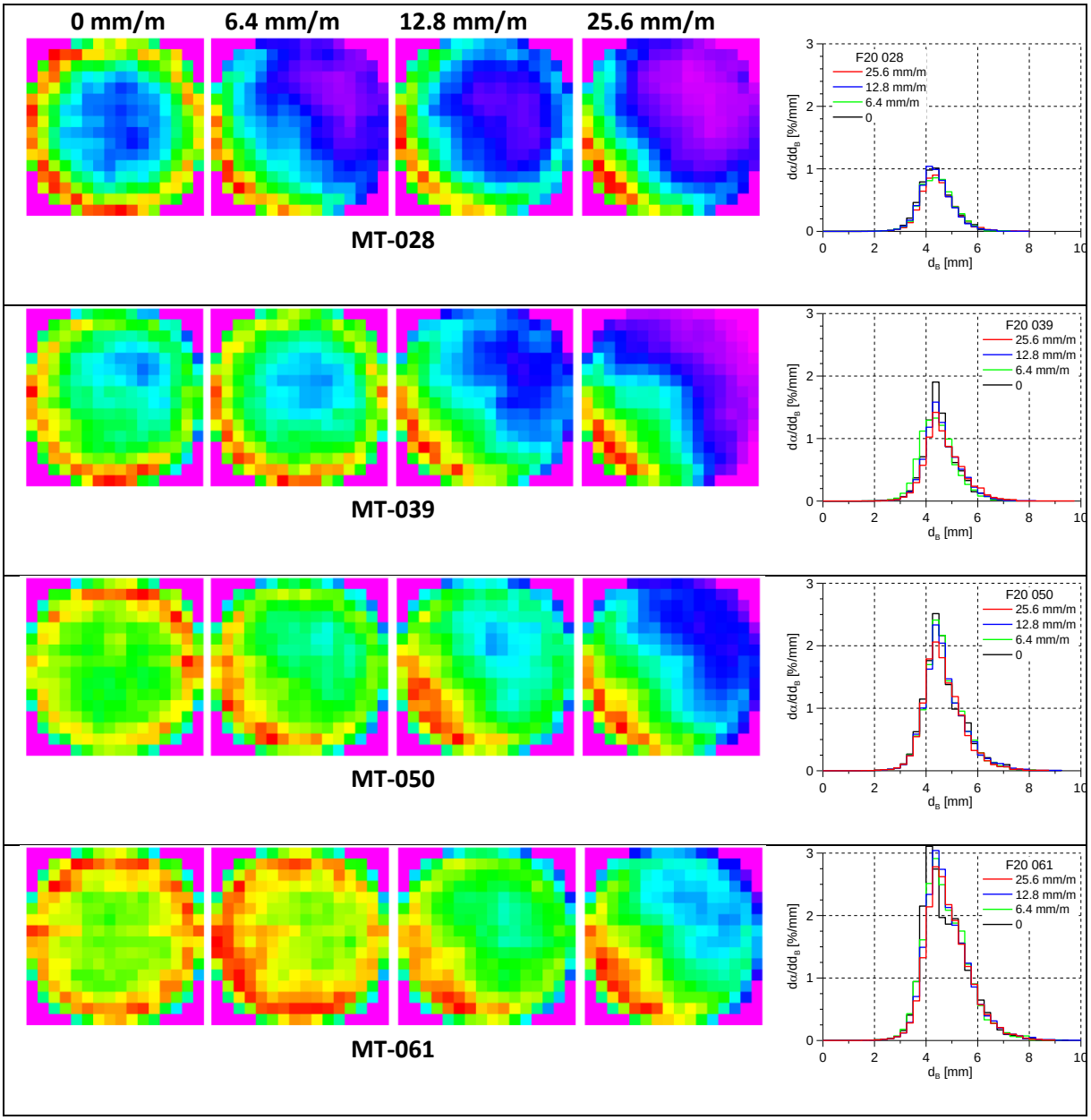

Figure 14: Measured gas fraction distributions (left) and bubble size distributions (right) at the end of the investigated pipe for inclinations of 0, 6.4, 12.8 and 25.6 mm/m (left to right)

7.2. Calculations and discussion

The simulations are performed with the models described in section 2, including the values of all constants. In the present application the axial symmetry is disturbed. Hence, as before a fully 3D simulation of the 3 m pipe with a diameter of 0.0512 m is applied. The same hexahedral grid with about 470000 cells is used. The inclination is realized in positive y-direction for the quite small values 6.4 mm/m, 12.8 mm/m and 25.6 mm/m. The monodispersed approach is justified by the non-changing bubble size distribution also for the strongest investigated inclination (see right side of Figure 14 in section 7.1).

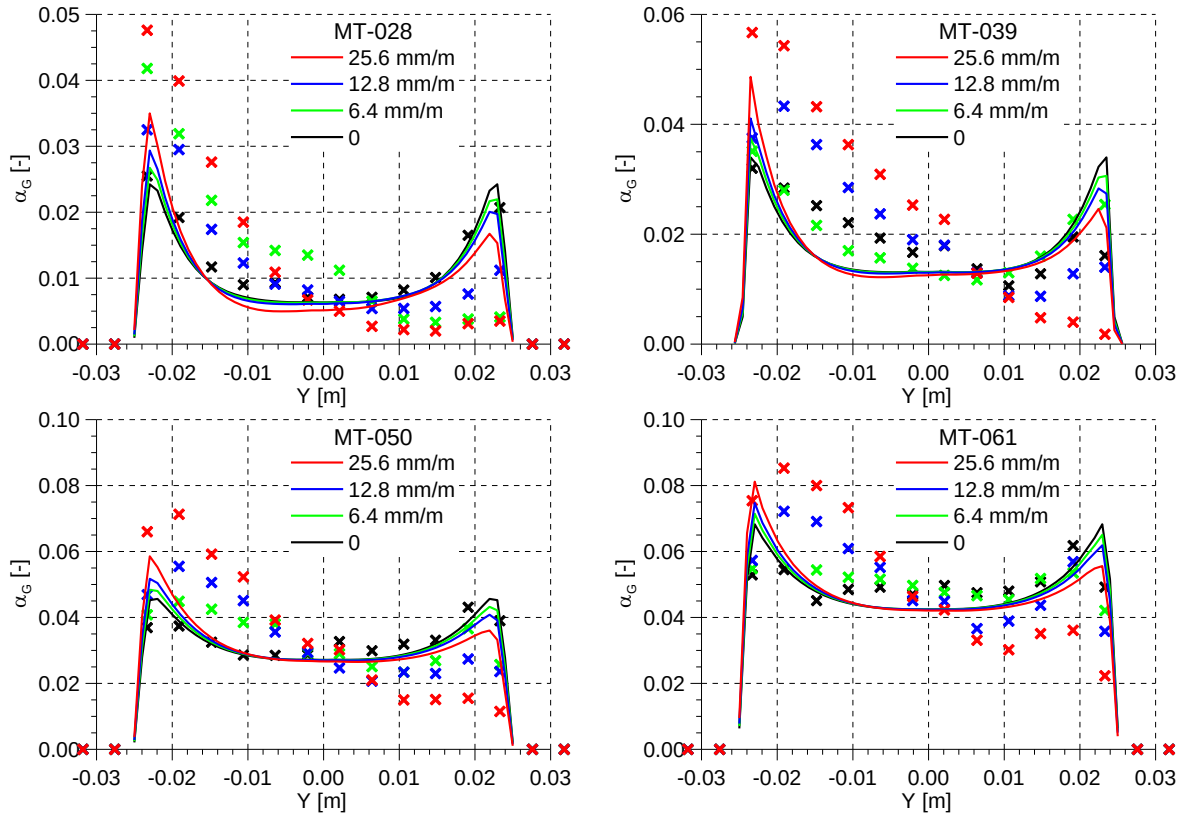

Figure 15: Measured (stars) and calculated (solid lines) gas fraction profiles in slightly inclined pipes

The gas fraction profiles of Figure 15 show an increased asymmetry with increasing inclination. The comparison to the measurements represents the correct tendencies but the effect is strongly under-predicted.

7.3. Investigation of model variations

The analysis of the value of the acting non-drag forces (see Figure 16) shows a large contribution from the lift force which should be subjected to a closer examination. This is the topic of the present investigation.

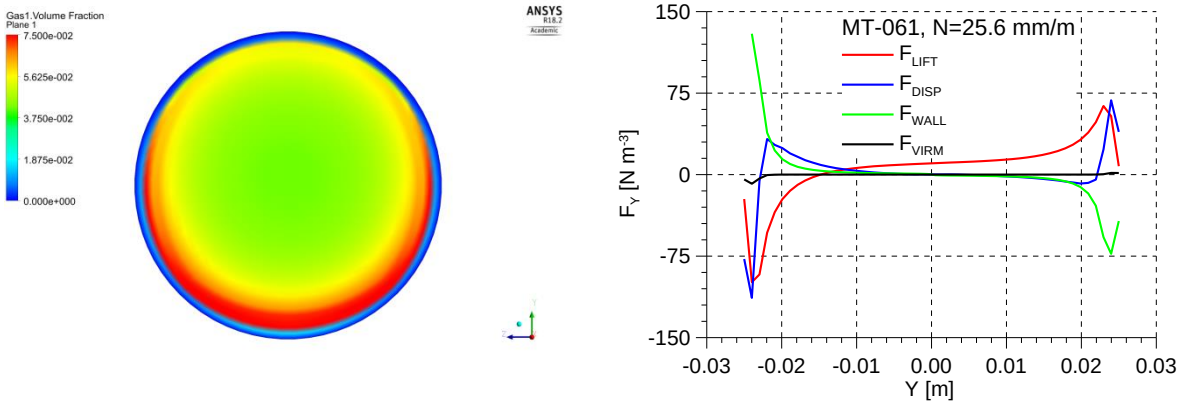

Figure 16: Calculated cross sectional distribution of gas fraction (left side) and non-drag forces (right) at 3.03 m upstream the gas injection for the test MT-061 with an inclination of 25.6 mm/m

In the literature many discussions on the lift force can be found (e.g. Ziegenhein at al. 2013). The correlation by Tomiyama (2002) applied here (see. Eq. (5), section 2.1.2) was obtained based on experiments with single bubbles in a laminar linear shear field in highly viscous liquids. Nevertheless, air-water and steam-water experiments showed a good agreement of this correlation at least for the critical diameter where the lift force changes its sign (Lucas and Tomiyama, 2011). Even in wall boiling tests in refrigerants (namely the DEBORA tests using R12) some observed phenomena could be explained by applying this lift correlation (Krepper et al. 2013). A main feature of the correlation by Tomiyama (2002) is that the lift coefficient decreases with increasing deviation of the bubble shape from spherical as the bubble sizes increases. At a certain critical size a sign change occurs (see Figure 1 in section 2.1.2).

To investigate this effect more in detail, recently experiments on lift force for low viscous systems (air-water and air-water + additives) were conducted at HZDR. To this end a new experimental methodology was developed (Ziegenhein 2016, Ziegenhein et al., 2018). Preliminary results show that the Tomiyama correlation agrees well also for such conditions in case the modified Eötvös number is calculated based on the true measured bubbles major axis (Figure 17).

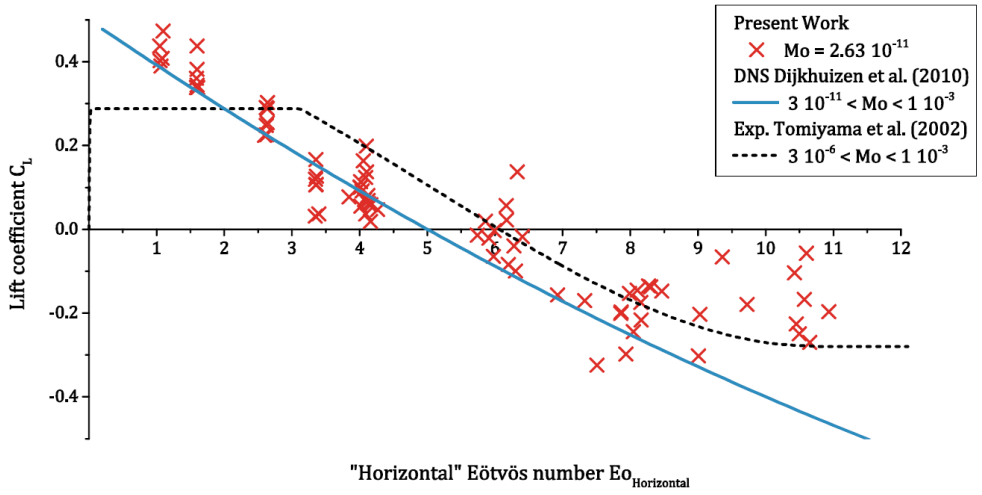

Figure 17: Experimentally determined lift force coefficient for air water-system (x) based on the modified Eötvös number in comparison with DNS results obtained by Dijkhuizen et al. (2010) and the Tomiyama (2002) correlation (from Ziegenhein at al., 2018).

The bubble major axis in most cases is calculated by the correlation by Wellek (1966) Eq. (7), which, however, was obtained for contaminated systems. A bubble shape correlation, which fits for many experimental air-water data was published by Ziegenhein et. al. (2017), namely

$$d_{\perp} = d_B \sqrt[3]{1+1.5 \cdot Eo^{0.3}} \tag{22}$$

A set of simulations was performed where the lift force was modeled based on Eq. (22). In Figure 18 this new set of simulations, denoted by $F_{LIFT}2$, is compared to the previous one, denoted by $F_{LIFT}1$, where the lift force was calculated based on Eq. (7). The tendencies calculated by $F_{LIFT}2$ correspond much better to the measurements than for $F_{LIFT}1$.

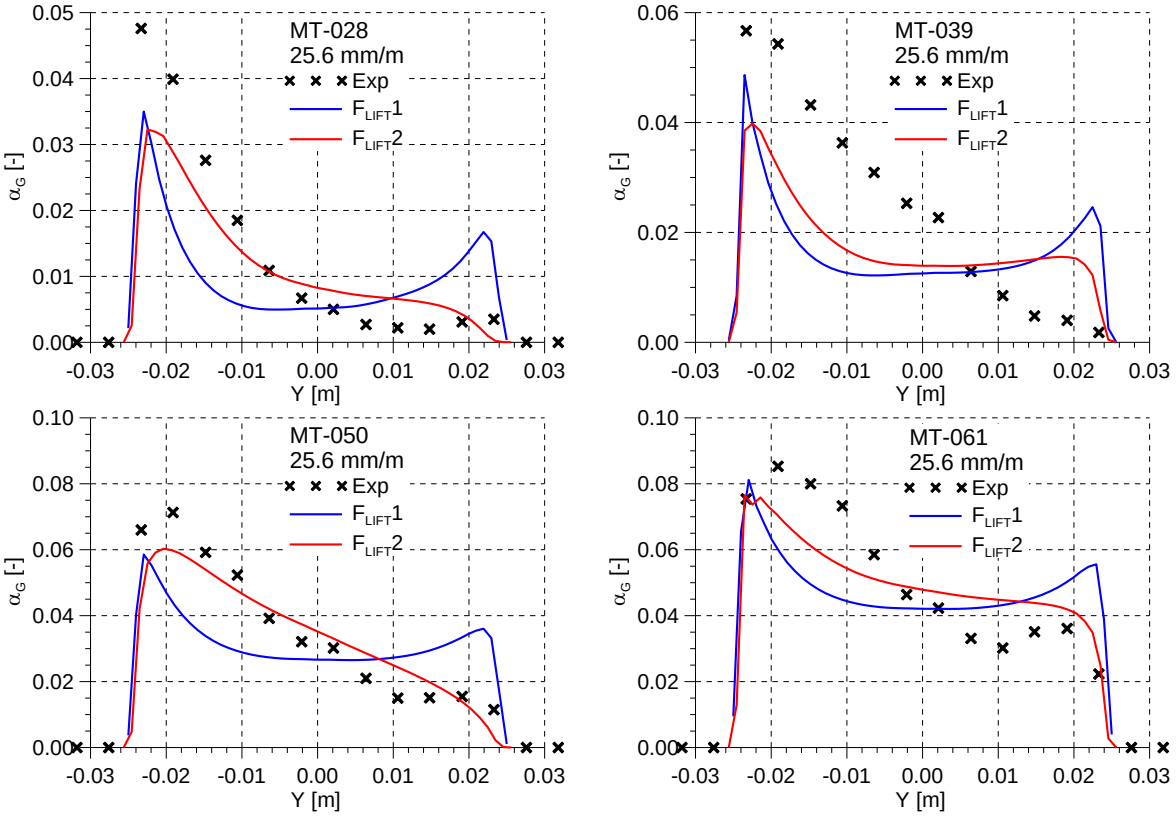

Figure 18: Effect of lift force model on the gas fraction profile (N = 25.6 mm/m)

8. SUMMARY AND CONCLUSIONS

The CFD simulation of two-phase bubbly flow in an industrial scale requires the definition of closure models for bubble forces, bubble-induced turbulence and bubble coalescence and breakup. In the present paper concentrating on tests with low gas fraction the latter issue was excluded. The model development and validation work is in many cases based on developed bubbly flow in vertical upward pipes. In the present paper the developed models were applied in addition also for the description of other flow phenomena.

For bubbly flow in a vertical pipe at limited gas fraction the radial gas profiles are mainly determined by the interplay of lift- turbulent dispersion- and wall force. For developed flows the virtual mass force plays no role. With increasing gas fractions the turbulent dispersion force becomes larger. Then the radial gas profiles are determined by the interplay of turbulent dispersion force and wall force.

For the development of the gas fraction distribution behind the gas injection by nozzles besides the lift- and the turbulent dispersion force also the virtual mass force plays an important role. With the presented framework of drag and non-drag force components the general properties of the gas fraction profiles could be described with good agreement to the experiments, e.g. the signature of the nozzle location disappeared in the calculations about at the same level as in the experiments. The exact shape of the profile is influenced very sensitively via the lift force by the velocity field and the exact simulation of the sparger plays an important role.

Also in the slightly inclined pipe the general development of the flow asymmetries could be described with qualitative agreement to the measurement, but qualitatively a significant underestimation of the phenomenon was found. The analysis of the bubble forces shows the lift force contributing an important part. Model variations resulting in a slightly smaller contribution of lift-force were investigated. These variations improved the agreement of the calculated gas fraction profiles to the measurements. For a clear statement further investigations are necessary. Especially it must be shown that the model deviations do not worsen the simulation of other flow regimes and other observables.

The main purpose of the present paper is to show the capability of the presented model framework to simulate different situations of bubbly flow with good agreement to experiments. CFD serves here as a tool to visualize the model elements like non-drag forces and demonstrate their plausible interaction.

The goal of the model development is a model framework to be able to predict a flow situation dependent on a given boundary condition. The investigations show that for a bubbly flow in a pipe the specification of the liquid and gas superficial velocity are not sufficient as boundary conditions. The bubble size plays an important role. Momentum exchange relations very sensitive depend on the bubble size. For heat and mass transfer between the phases (not considered in the present work) the interfacial area density - related to the bubble size - is an important parameter.

Already the consideration of an averaged value for the bubble size in a monodispersed approach can improve the predicting capabilities. A further improvement can be gained by consideration of the distribution of bubble size, which is possible by a fixed polydispersed approach (Rzehak and Krepper 2015). A complete description of the two-phase flow behaviour would require also the description of bubble coalescence and fragmentation. The actual models for the latter phenomenon however are still far away from a predictive level of maturity.

9. NOMENCLATURE

Notation	Unit	Denomination
C_D	-	drag coefficient
C_L	-	lift coefficient
C_{TD}	-	turbulent dispersion coefficient
C_{VM}	-	virtual mass force coefficient
C_W	-	wall force coefficient
C_μ	-	shear-induced turbulence coefficient (k-ε model)
C_{kB}	-	coefficient for k-source due to bubble-induced turbulence
$C_{\varepsilon B}$	-	coefficient for ε-source due to bubble-induced turbulence
d_B	m	bulk bubble diameter
$d_{B,Ref}$	m	reference bubble diameter at normal conditions
$d_\perp$	m	bubble diameter perpendicular to main motion
D	m	pipe / column diameter or width
Eo	-	Eötvös Number
$\mathbf{F}$	N m^{-3}	force
$\mathbf{g}$	m s^{-2}	acceleration of gravity
H	m	pipe length / column height
J	m s^{-1}	superficial velocity = volumetric flux
k	m^2 s^{-2}	turbulent kinetic energy
ℓ	m	characteristic eddy size
Mo	-	Morton Number
P	Pa	pressure
P_{REF}	Pa	Reference pressure
r	m	radial coordinate
R	m	pipe / column radius or half-width
Re	-	Reynolds number
t	s	time
$\mathbf{T}$	N m^{-2}	stress tensor
$\mathbf{u}$	m s^{-1}	velocity
u_τ	m s^{-1}	friction velocity
U	m s^{-1}	velocity scale

u'	m s^{-1}	fluctuation velocity
x	m	axial coordinate
y	m	wall normal coordinate
z	m	spanwise coordinate
α	-	phase fraction
δ	m	viscous length scale
ε	m^2 s^{-3}	turbulent dissipation rate
μ	kg m^{-1} s^{-1}	dynamic viscosity
ν	m^2 s^{-1}	kinematic viscosity
ρ	kg m^{-3}	density
σ	N m^{-1}	surface tension
τ_W	N m^{-2}	wall shear stress
ω	s^{-1}	characteristic eddy frequency

10. REFERENCES

Auton, T., Hunt, J., Prud'Homme, M., 1988. The force exerted on a body in inviscid unsteady non-uniform rotational flow. Journal of Fluid Mechanics 197, 241.

Burns, A.D., Frank, T., Hamill, I., Shi, J.-M., 2004. The Favre averaged drag model for turbulence dispersion in Eulerian multi-phase flows. Proc. 5th Int. Conf. on Multiphase Flow, ICMF2004, Yokohama, Japan, 2004.

Dijkhuizen, W., Roghair, I., Annaland, M. V. S., Kuipers, J., 2010. DNS of gas bubbles behaviour using an improved 3D front tracking model - Drag force on isolated bubbles and comparison with experiments. Chemical Engineering Science, 65, 1415

Drew, D. A., Passman, S. L., 1998. Theory of Multicomponent Fluids. Springer.

Hosokawa, S., Tomiyama, A., Misaki, S. and Hamada, T., 2002. Lateral migration of single bubbles due to the presence of wall. Proc. ASME Joint U.S.-European Fluids Engineering Division Conference, In: FEDSM 2002, Montreal, Canada

Ishii, M., Zuber, N., 1979. Drag coefficient and relative velocity in bubbly, droplet or particulate flows, AIChE J. 25, 843.

Ishii, M., Hibiki, T., 2011. Thermo-fluid dynamics of two-phase flow. Springer, 2nd ed.

Krauß, M., Rzehak, R., 2018. Reactive absorption of CO2 in NaOH: An Euler-Euler simulation study. Chemical Engineering Science, 181, 199-214

Krepper, E., Beyer, M., Lucas, D. and Schmidtke, M., 2011. A population balance approach considering heat and mass transfer-Experiments and CFD simulations. Nuclear Engineering and Design, 241, 2889- 2897

Krepper, E., Rzehak, R., Lifante, C. and Frank, T., 2013. CFD for subcooled flow boiling: Coupling wall boiling and population balance models. Nuclear Engineering and Design, 255, 330- 346

Liao, Y.; Rzehak, R.; Lucas, D. , Krepper, E., 2015. Baseline closure model for dispersed bubbly flow: Bubble-coalescence and breakup. Chemical Engineering Science, 122, 336-349

Lucas, D.; Krepper, E., Prasser, H.-M., 2005. Development of co-current air-water flow in a vertical pipe. International Journal of Multiphase Flow, 31, 1304-1328

Lucas, D., Krepper, E., Prasser, H.-M., 2007. Use of models for lift, wall and turbulent dispersion forces acting on bubbles for poly-disperse flows. Chemical Engineering Science 62, 4146.

Lucas, D., Tomiyama, A., 2011. On the role of the lateral lift force in poly-dispersed bubbly flows. International Journal of Multiphase Flow, 37, 1178.

Lucas, D.; Rzehak, R.; Krepper, E.; Ziegenhein, T.; Liao, Y.; Kriebitzsch, S. , Apanasevich, P., 2016. A strategy for the qualification of multi-fluid approaches for nuclear reactor safety. Nuclear Engineering and Design, 299, 2-11

Ma, T., Santarelli, C., Ziegenhein, T., Lucas, D. , Froehlich, J., 2017. Direct numerical simulation–based Reynolds-averaged closure for bubble-induced turbulence. Physical Review Fluids, 2, 034301

Magnaudet, J., Rivero, M., Fabre, J., 1995. Accelerated flows past a rigid sphere or a spherical bubble Part 1: Steady straining flow. Journal of Fluid Mechanics, 284, 97.

Menter, F., 1994. Two-equation eddy-viscosity turbulence models for engineering applications, AIAA-Journal 32, 1598.

Menter, F. R., 2009. Review of the shear-stress transport turbulence model experience from an industrial perspective. International Journal of Computational Fluid Dynamics 23, 305-316.

Rzehak, R.; Krepper, E. , Lifante, C., 2012. Comparative study of wall-force models for the simulation of bubbly flows. Nuclear Engineering and Design, 253, 41-49

Rzehak, R., Krepper, E., 2013a. Bubble-induced turbulence: Comparison of CFD models. Nuclear Engineering and Design, 258, 57-65

Rzehak, R., Krepper, E., 2013b. Closure models for turbulent bubbly flows: A CFD study. Nuclear Engineering and Design, 265, 701–711

Rzehak, R., Krepper, E., 2013c. CFD modeling of bubble-induced turbulence. International Journal of Multiphase Flow, 55, 138–155

Rzehak, R., Krepper, E., 2015. Bubbly flows with fixed polydispersity: validation of a baseline closure model. Nuclear Engineering and Design, 287, 108-118

Rzehak, R.; Krepper, E.; Liao, Y.; Ziegenhein, T.; Kriebitzsch, S., Lucas, D., 2015. Baseline model for the simulation of bubbly flows. Chemical Engineering and Technology, 38, 1972-1978

Rzehak, R., Krepper, E., 2016. Euler-Euler simulation of mass-transfer in bubbly flows. Chemical Engineering Science 155, 459–568.

Rzehak, R.; Ziegenhein, T.; Kriebitzsch, S.; Krepper, E., Lucas, D., 2017a. Unified modeling of bubbly flows in pipes, bubble columns, and airlift columns. Chemical Engineering Science, 157, 147-158

Rzehak, R., Krauß, M., Kovats, P., and Zähringer, K., 2017b. Fluid dynamics in a bubble column: New experiments and simulations. International Journal of Multiphase Flow 89, 299–312.

Tomiyama, A., Sou, A., Zun, I., Kanami, N., Sakaguchi, 1995. Effects of Eötvös number and dimensionless liquid volumetric flux on lateral motion of a bubble in a laminar duct flow. Proc. 2nd Int. Conf. on Multiphase Flow, Kyoto, Japan, 3.

Tomiyama, A., Kataoka, I., Zun, I., Sakaguchi, T., 1998. Drag coefficients of single bubbles under normal and micro gravity conditions. JSME International Journal B 41, 472.

Tomiyama, A., Tamai, H., Zun, I., Hosokawa, S., 2002. Transverse migration of single bubbles in simple shear flows. Chemical Engineering Science 57, 1849.

Wellek, R.M., Agrawal, A.K., Skelland, A.H.P., 1966. Shapes of liquid drops moving in liquid media. AIChE Journal 12, 854.

Wilcox, D. C., 1998. Turbulence modeling for CFD. DCW-Industries.

Yeoh, G. H., Tu, J. Y., 2010. Computational techniques for multiphase flows — basics and applications. Butterworth-Heinemann, Elsevier Science and Technology.

Ziegenhein, T., Rzehak, R., Krepper, E. and Lucas, D., 2013. Numerical simulation of polydispersed flow in bubble-columns with the inhomogeneous multi-size-group model. Chemie Ingenieur Technik, 85, 1080-1091

Ziegenhein, T., 2016. Fluid dynamics of bubbly flows. PhD-Thesis TU Berlin

Ziegenhein, T., Rzehak, R., Ma, T. Lucas, D. 2017. Towards a unified approach for modeling uniform and non-uniform bubbly flows. Canadian J. Chem. Eng., 95, 170–179

Ziegenhein, T., Tomiyama, A., Lucas, D. 2018. A new measuring concept to determine the lift force for distorted bubbles in low Morton number system: Results for air/water. Int. J. Multiphase Flow, submitted

Zun, I. 1980., The transverse migration of bubbles influenced by walls in vertical bubbly flow. International Journal of Multiphase Flow 6, 583.